EPJ manuscript No.
(will be inserted by the editor)

arXiv:1604.00248v2 [cond-mat.stat-mech] 2 Dec 2016

Nonequilibrium dynamics of the three-dimensional Edwards-Anderson spin-glass model with Gaussian couplings: strong heterogeneities and the backbone picture

F. Romá[1], S. Bustingorry[2], and P. M. Gleiser[2]

[1] Departamento de Física, Universidad Nacional de San Luis, INFAP, CONICET, Chacabuco 917, D5700BWS San Luis, Argentina
[2] CONICET, Centro Atómico Bariloche, R8402AGP San Carlos de Bariloche, Río Negro, Argentina

Received: date / Revised version: December 5, 2016

Abstract. We numerically study the three-dimensional Edwards-Anderson model with Gaussian couplings, focusing on the heterogeneities arising in its nonequilibrium dynamics. Results are analyzed in terms of the backbone picture, which links strong dynamical heterogeneities to spatial heterogeneities emerging from the correlation of local rigidity of the bond network. Different two-times quantities as the flipping time distribution and the correlation and response functions, are evaluated over the full system and over high- and low-rigidity regions. We find that the nonequilibrium dynamics of the model is highly correlated to spatial heterogeneities. Also, we observe a similar physical behavior to that previously found in the Edwards-Anderson model with a bimodal (discrete) bond distribution. Namely, the backbone behaves as the main structure that supports the spin-glass phase, within which a sort of domain-growth process develops, while the complement remains in a paramagnetic phase, even below the critical temperature.

PACS. 75.10.Nr Spin-glass and other random models – 75.40.Gb Dynamic properties (dynamic susceptibility, spin waves, spin diffusion, dynamic scaling, etc.) – 75.40.Mg Numerical simulation studies – 75.50.Lk Spin glasses and other random magnets

1 Introduction

The idea that different structures with a conventional physical behavior are hidden inside of a disordered and frustrated material, is not new. Historically this approach was one of the earliest considered in order to make a simple and intuitive picture of spin glasses [1,2]. Although superparamagnetism [3,4] is a crude approximation of a spin-glass system, since it assumes the existence of independent non-interacting magnetic clusters with some kind of internal magnetic order, for many years experimental data were interpreted within this theoretical framework. This was not a capricious choice: Experiments at temperatures far above the freezing temperature T_f, e. g., dc-susceptibility measurements, can easily be understood in these terms [5].

For temperatures close or below T_f, the experimental evidence indicates that such description is still possible if a spin glass is supposedly formed by interacting clusters or "building blocks" of spins [2]. Some attempts were made to explore this possibility (see Ref. [1]). For example, a phenomenological and intuitive picture has been proposed to explain several experimental results on canonical spin glasses [2,6]. The clusters are defined as groups of spins linked by exchange bonds stronger than the thermal energy. Considering RKKY interactions [7,8,9] between these spins, it is possible to delineate structures which grow as the temperature decreases. At T_f an infinite-correlated cluster (a "dynamic backbone") emerges and percolation-like features can be identified.

Such simple theories have been displaced by others, as the mean field [10,11] and the droplet [12] pictures. Partly because latter theoretical frameworks allow to derive analytical expressions for different quantities characterizing the physical behavior of a spin glass which, in principle, could be verified by comparing with experimental and numerical evidence. Also, because the experience gained from numerical simulation indicates that these clusters, built on the basis of a "local energy criterion", are not adequate to describe such disordered and frustrated systems. Nevertheless, despite the great theoretical progress made so far, the controversy about the nature of the spin-glass phase remains unresolved.

In this context, it is not surprising that the efforts to describe the spin-glass problem in terms of magnetic clusters still persist. They are encouraged both by the experimental data, and the observation of strong spatial heterogeneities in numerical simulations of model systems. Such is the case of the Edwards-Anderson model [13] with bimodal couplings [14]. The ground state of this system is

highly degenerated enabling to separate the lattice into two regions, one that contributes to the degeneration and other that remains unchanged in all ground states. The latter, known as the "rigid lattice"[15], is a good candidate for a magnetic backbone capable of sustaining order in the system and has been the subject of various topological studies [15,16,17,18,19]. In recent years, our understanding of the role played by this structure has advanced considerably. In fact, for the case of the Edwards-Anderson model with bimodal couplings, spatial heterogeneities characterized by the rigid lattice have been associated to the equilibrium and nonequilibrium response of the system [20,21,22,23,24,25,26].

These studies have resulted in a generalization of the cluster approach for spin glasses (and for other systems with quenched disorder), appropriately named the "backbone picture" [24,27]. The main conjecture of this picture is that it is possible to define an "effective interaction" between a pair of spins at sites i and j, different from the bond strength J_{ij}. This quantity is the rigidity r_{ij}, which accounts for the energetic cost to leave the bond's state in the ground state (satisfied or frustrated).

The rigid structure is defined as the lattice where each bond J_{ij} is replaced by its corresponding rigidity r_{ij}. This can be accessed for spin-glass models with Ising spin variables [24,27], based on the ground-state configurations and the low-excitation levels. In particular, in Ref. [27] the topological properties of the rigid structure were studied for the Edwards-Anderson model with both bimodal and Gaussian bond distributions, in two and three-dimensions. There, it was also analyzed how the spatial heterogeneities, characterized by the rigid structure, influence the equilibrium properties of these models at finite temperature. The results show that any disordered sample can be divided into two sectors, the backbone and its complement, and that within these regions the physical behaviors are very different. What remains to be studied is how the rigid structure influences the nonequilibrium dynamics of the Edwards-Anderson model with Gaussian couplings. In order to fill this gap, in this work we study by means of Monte Carlo simulations, the nonequilibrium dynamical heterogeneities of the three-dimensional Edwards-Anderson spin-glass model with Gaussian couplings within the framework given by the backbone picture. Different two-times quantities, as the flipping time distribution and the correlation and response functions, are analyzed. We find that the dynamical heterogeneities can be clearly associated to the rigid structure.

The paper is structured as follows. In Sec. 2 we present the Edwards-Anderson spin-glass model. We also summarize the most important properties of its rigid structure and we introduce the concept of the backbone. Then, an extensive numerical simulation study of the nonequilibrium dynamics of this system is presented in Sec. 3. It is shown that different observables as the mean flipping time distribution, the correlation and the integrated response functions, as well as the fluctuation-dissipation plots, behave very differently if they are evaluated inside or outside the backbone. In the last section we discuss our results and conclusions are drawn.

2 The Edwards-Anderson spin-glass model and its ground state rigid structure

We start by considering the three-dimensional (3D) Edwards-Anderson spin-glass model [13] with Gaussian couplings (EAG), which consists of a set of N Ising spins $\sigma_i = \pm 1$ placed in a cubic lattice of linear dimension L ($N = L^3$), with periodic boundary conditions in all directions. The Hamiltonian is

$$H = -\sum_{(i,j)} J_{ij}\sigma_i\sigma_j, \tag{1}$$

where (i,j) indicates a sum over the six nearest neighbors. The coupling constants or bonds, J_{ij}, are independent random variables drawn from a Gaussian distribution with mean value zero and variance one. The EAG model undergoes a continuous phase transition at a critical temperature $T_c \approx 0.95$ [28,29] (temperatures are given in units of $1/k_B$, where k_B is Boltzmann's constant).

Since the rigid structure and the backbone play a central role in this work, now we give a brief summary of how these concepts have evolved in the last few years. A more detailed discussion can be found in Refs. [24,27].

For the simpler version of the model, the Edwards-Anderson spin-glass model with bimodal $\pm J$ couplings (EAB) [14], the ground state (GS) is multiply degenerated and then it is trivial to define a backbone. Bonds which do not change its condition (satisfied or frustrated) in all the configurations of the GS, are called "rigid bonds" and form the "rigid lattice" [15]. This structure of bonds and the set of spins connected by them constitute the so called backbone of the system. The remaining bonds are called "flexible bonds" and form the "flexible lattice".

The backbone of the EAB model has some remarkable topological properties that have been carefully evaluated through numerical simulations. For two-dimensional (2D) square lattices, numerical results are affected by significant finite size effects but show that the most likely scenario is that this structure does not percolate in the thermodynamic limit (another possibility is that the backbone is just located on the percolation threshold). This backbone is fragmented into several clusters whose size distribution exhibits a power-law dependence, and the estimated critical exponents are consistent with the 2D random percolation universality class [30]. On the other hand, for the 3D cubic lattice both sets, the backbone and its complement, percolate the system but with critical exponents differing from those within the 3D random percolation universality class.

More interesting is the connection between the backbone structure and the nonequilibrium dynamical behavior. Both, the 2D and the 3D EAB models have a very broad distribution of relaxation times which, at low temperatures, show a spontaneous time-scale separation enabling to split the system in two sets, one consisting of

"fast" spins and another of "slow" spins [31]. It was shown that these fast and slow degrees of freedom are directly related to spins outside and inside the backbone structure, respectively [20,23]. Furthermore, numerical simulations [32,33] show that below its critical temperature the 3D EAB model exhibits a violation of the fluctuation-dissipation theorem (FDT) that, in the framework of mean field theory, resembles the full replica-symmetry breaking solution [34,35]. We had previously shown that for very long simulation times spins outside the backbone satisfy the FDT, whereas those within the backbone violate this relation [22]. Therefore, from a topological and dynamical point of view and below the critical temperature, a spin glass can be thought of as consisting of two different sets, one associated with an ordered-like phase (the backbone) and another with a disordered paramagnetic-like phase (the complement of backbone). Such results for the EAB model are not trivial. In addition, a similar phenomenon is probably taking place in other spin-glass systems such as the 2D $\pm J$ Potts model [36] and the Viana-Bray model [37] as suggested by numerical results.

Notice that the definition of backbone based on the rigid lattice as used for the EAB model, is not appropriate for systems with a simply degenerated GS, since then the backbone structure would include the entire lattice. Such is the case of the EAG model which has a zero-entropy fundamental level (with only two configurations related by a global spin-flip) [38]. In order to address the case of Ising models with simple degenerated GSs, a generalization of the concept of rigidity was presented in Refs. [24, 27]. The definition of backbone is then based on the following concepts. The first key idea is to consider not only the GS but also the low-excitation levels. The "rigidity" of each bond should be a parameter taking a continuum of values, instead of only two (rigid-flexible) as in the EAB model. Let us consider a sample (a particular realizations of bond disorder) of the Edwards-Anderson model with an arbitrary bond distribution (discrete or continuous). For each bond J_{ij} we define its rigidity as $r_{ij} = U_{ij} - U$, where U is the GS energy of the sample and U_{ij} is the lowest energy for which the bond J_{ij} changes its GS condition (from satisfied to frustrated or vice versa). In other words, such bond does not change (remains rigid) for all configurations with energy lower than $r_{ij} + U$. The "rigid structure" (RS) of a sample is then defined as the lattice where each bond J_{ij} has been replaced by its rigidity r_{ij}. According to the backbone picture, the latter is a quantity that gives the magnitude of the "effective interaction" between the pair of spins at sites i and j.

The RS for both the EAB and the EAG models, can be numerically determined using a method proposed in Refs. [24,39]. For this approach to work properly, it is necessary to find many low-lying energy configurations for each sample. For the EAG model the number of configurations one needs to determine is of the order of the number of bonds in the system. In Ref. [27], a parallel tempering Monte Carlo algorithm [40,41] was used for this purpose. This technique, widely used in equilibrium simulations, also provides a powerful heuristic method for reaching

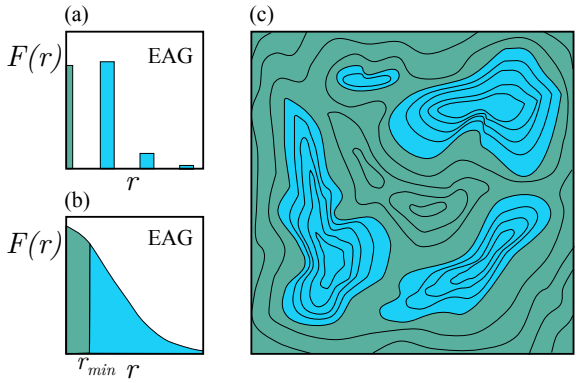

Fig. 1. Rigidity distribution for the (a) EAB and (b) EAG models. Different colors indicate rigidities below and above the threshold value, $r_{\min}$. (c) Two dimensional schematic picture of the spatial distribution of rigidity values. Lines correspond to contour levels while the colors indicate high and low rigidity regions according to the rigidity distributions shown in (a) and (b).

the GS of spin-glass models [42,43]. Nevertheless, because the calculation of GS configurations of the 3D Edwards-Anderson model is an NP-hard problem, in practice the RS can be numerically determined only for samples of small size. In particular, for the 3D EAG model, the parallel tempering algorithm allows one to obtain GSs with a high probability for lattice sizes up to $L = 10$ [43]. Since $3N$ of such configurations are required to calculate the RS of a single sample, we restrict our analysis to $L = 8$ [27].

The interpretation of the rigidity r_{ij} as an effective interaction is the basis on which rests a generalized definition of the backbone. Given the random distribution of bonds, the rigidity distribution $F(r)$, where $F(r)dr$ is the fraction of bonds whose rigidities are between r and $r+dr$, can be computed. The results, taken from Ref. [27], are shown in Figs. 1(a) and (b) for the 3D EAB and EAG models, respectively. For the EAB model the rigidity distribution is discrete and bonds with non-zero rigidity [$r = 4$, $r = 8$, and $r = 12$, indicated with a different color in Fig. 1(a)] have similar physical behaviors. Thus, naturally, they are considered as parts of a single set, determining the main physical behavior, which we call the backbone. The remaining bonds with $r = 0$, behave in a very different way and are considered outside this set.

For the EAG model the rigidity is a continuous variable and the rigidity distribution takes the continuum form presented in Fig. 1(b). Since we expect that the physical behavior of the 3D Edwards-Anderson model should not depend on the exact form of the bond distribution, then even for this continuous rigidity distribution it should be possible to divide the system into two parts with different physical properties: the backbone and its complement. In fact, as shown in Ref. [27], in 2D a rigidity threshold value $r_{\min}$ can be found to separate the system into high-rigidity (HR) and low-rigidity (LR) components such that the EAB and the EAG models share the same percolation properties and have a similar equilibrium behavior.

For example, a $r_{\min}$ value can be selected such that a similar temperature dependence of the average energy per bond within each region for the EAB and the EAG models can be obtained. Therefore, bonds within the HR region (which has $r \geq r_{\min}$) form the backbone of the system. Furthermore, this idea can be extended to 3D, where following these same criteria the numerical data suggest that a suitable backbone could be defined for $0.6 < r_{\min} < 2.0$. Based on these results, and also to minimize frustration within the HR region, we use here the value $r_{\min} = 1.3$ (which was already used in Ref. [27]). Moreover, it is important to highlight that by choosing values of $r_{\min}$ in the range $0.6 - 2.0$ we obtain qualitatively similar results (as discussed in the next Section and in the Appendix), thus not changing our main findings.

We stress that although bond values are randomly distributed on the sample, rigidity values are spatially correlated. In Fig. 1(c) the spatial distribution of rigidity values are schematically shown using contour levels and with colors indicating HR and LR regions. Note that this figure is a schematic representation introduced with the intention of presenting the main ideas leading to a backbone picture (the map plots in figure 2 of Ref. [27], show actual images of the spatial distribution of rigidity in 2D). In the framework of this phenomenological theory, we emphasize that bonds and spins within these regions should display different dynamical behaviors.

In the following section, we study the strong heterogeneities arising in the nonequilibrium dynamics of the 3D EAG model, by evaluating different spin observables over the full (all spins), the HR (spins connected by bonds with $r \geq r_{\min} = 1.3$), and the LR (remaining spins) regions. To this end, we use the same set of 10^3 samples of $L = 8$ considered in Ref. [27], for which the corresponding RSs have already been calculated.

3 Numerical results

In order to investigate the nonequilibrium dynamics of the 3D EAG model, we use a typical protocol which consists on a quench at time $t = 0$ from a random configuration to a low temperature T below T_c. From this initial condition, the evolution of the system is simulated by a single spin-flip Monte Carlo algorithm and different two-times quantities are analyzed, which depend on both the waiting time $t_{\rm w}$, when the measurement begins, and a given time $t > t_{\rm w}$. A unit of time consists of N elementary random spin-flip attempts. As stated above, in all cases cubic lattices of linear size $L = 8$ with full periodic boundary conditions were simulated. In addition, in some cases simulations on larger lattices of $L = 20$ were carried out in order to address finite size effects. The disorder average was performed over 10^3 different samples. Furthermore, for each sample we have averaged over 10 independent thermal histories (or runs), i.e., along different initial conditions and realizations of the thermal noise (except in subsection 3.2, where 10^4 of such runs were required to calculate the FDT map plots).

We simulate each sample for six temperatures between $T = 0.4$ and $T = 0.9$, for different waiting times up to $t_{\rm w} = 10^7$, and for a maximum time of $t = 2 \times 10^7$. Even for the highest temperature and within the longest time window, all observables calculated in this study depend on $t_{\rm w}$, indicating that our simulations are far from the equilibrium regime.

Hereinafter, we analyze the correlation and response functions, as well as the corresponding FDT plots. Then, the flipping time distribution for different temperatures and waiting times is studied.

3.1 Correlation and response functions

We begin by calculating the full two-times correlation function defined for $t > t_{\rm w}$ as

$$C(t, t_{\rm w}) = \left[\left\langle \frac{1}{N} \sum_{i=1}^{N} \sigma_i(t) \sigma_i(t_{\rm w}) \right\rangle \right]_{\rm av}, \qquad (2)$$

where $\langle \ldots \rangle$ represent an average over thermal histories and $[\ldots]_{\rm av}$ indicates average over disorder realizations. On the other hand, by adding to the Hamiltonian (1) a perturbation of the form $H_p = -\sum_{i=0}^{N} h_i \sigma_i$, with $h_i = \pm h$ being a random field of intensity h switched on at time $t_{\rm w}$, it is possible to calculate the full two-times integrated response function as [35]

$$\chi(t, t_{\rm w}) = \left[\left\langle \frac{1}{Nh} \sum_{i=1}^{N} \sigma_i(t)\ \mathrm{sgn}(h_i(t_{\rm w})) \right\rangle_h \right]_{av}. \qquad (3)$$

Here, the average $\langle \ldots \rangle_h$ should be taken over thermal histories of the perturbed system, and the value of h should be chosen small enough in order to reach the linear response regime. Nevertheless, instead of performing additional simulations with an applied field, we calculate χ for infinitesimal perturbations using the algorithm proposed in Refs. [33,44], which permits to determine the correlation and the response functions in a single simulation of the unperturbed system. This algorithm needs a Monte Carlo simulation implemented with a differentiable transition rate of the external field. Then, we use Glauber dynamics where local changes are accepted with a transition rate given by [45]

$$W_{\rm G} = \frac{\exp\left(-\beta \Delta H\right)}{1 + \exp\left(-\beta \Delta H\right)}, \qquad (4)$$

where $\beta = 1/T$ and ΔH is the energy change required to flip a given spin.

Figure 2 shows the dependence of the full correlation function C with $t - t_{\rm w}$, for $t_{\rm w} = 10^5$ at temperature $T = 0.6 < T_c$. Open (closed) black squares correspond to simulations for systems of size $L = 8$ ($L = 20$). From this comparison we conclude that finite-size effects are not important and then samples with $L = 8$, for which we know their RSs, represent very well the dynamic behavior

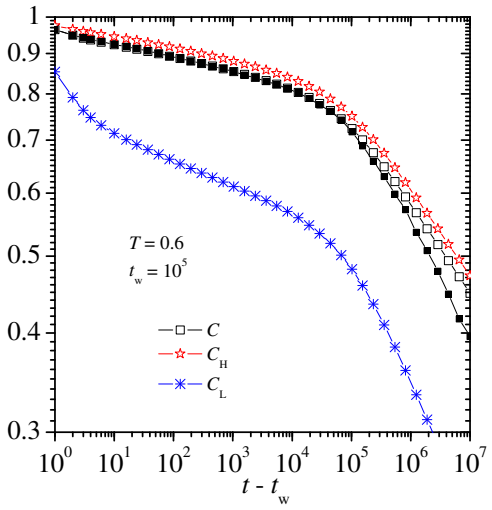

Fig. 2. The correlation functions C, $C_{\rm H}$, and $C_{\rm L}$ at $T = 0.6$ for the waiting time $t_{\rm w} = 10^5$. Closed black squares correspond to the full correlation function calculated for samples of size $L = 20$.

of the system. This is true for all quantities calculated in the following.

Most interesting is the heterogeneous behavior of this quantity. As we mentioned in the previous Section, each sample of the EAG system can be divided into the HR and LR regions. In addition to C, we then calculate the correlation function for the HR and the LR regions, $C_{\rm H}$ and $C_{\rm L}$ respectively, by restricting the sum in Eq. (2) to those spins belonging to each sector (and we normalize both sums using the corresponding number of spins of each region). Figure 2 shows that the behaviors of C and $C_{\rm H}$ are very similar, while $C_{\rm L}$ displays a more drastic initial relaxation followed by a second decay process as fast as the full correlation function.

Now, we analyze the dependence of correlation functions with the waiting time. Figure 3 (a) shows the full correlation function at $T = 0.6$. As expected, this quantity displays a typical aging behavior. Initially the correlation function slowly relaxes but, after a certain period of time, a faster relaxation process develops. With increasing $t_{\rm w}$ this second relaxation process begins at longer $t - t_{\rm w}$.

In Figs. 3 (b) and (c) we show the plots of $C_{\rm H}$ and $C_{\rm L}$ at temperature $T = 0.6$. While $C_{\rm H}$ shows the same evolution as C [compare with Fig. 3 (a)], with increasing waiting time the first decay of the correlation $C_{\rm L}$ becomes more pronounced, indicating that the spins within the LR region will be less correlated with time. This behavior is also observed in the nonequilibrium dynamics of 3D EAB model below its critical temperature [23], and indicates a significant difference between the backbone and its complement. As we mentioned in Section 2 and in the Appendix, by choosing values of $r_{\rm min}$ in $0.6 < r_{\rm min} < 2.0$ we obtain similar results.

The full integrated response function χ, as well as $\chi_{\rm H}$ and $\chi_{\rm L}$ (the responses of spins belonging to the HR and the LR regions) are shown, respectively, in Figs. 4 (a), (b),

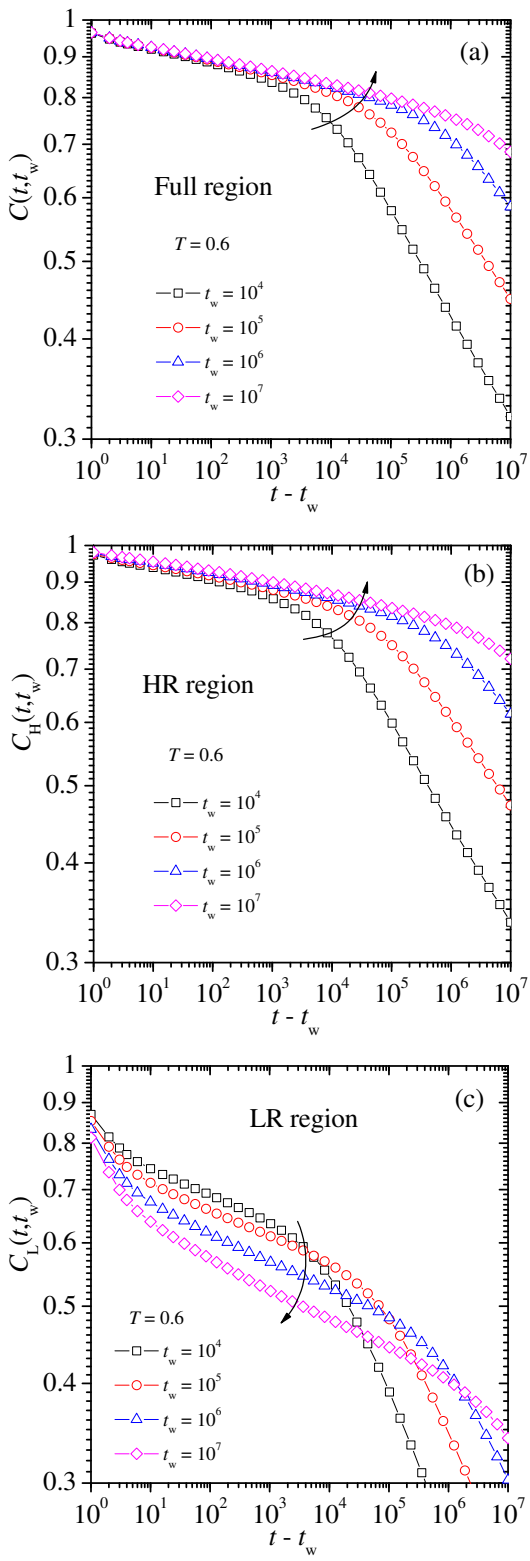

Fig. 3. The correlation functions (a) C, (b) $C_{\rm H}$, and (c) $C_{\rm L}$ at $T = 0.6$ and for different waiting times as indicated. The arrows emphasize how such functions evolve with increasing $t_{\rm w}$.

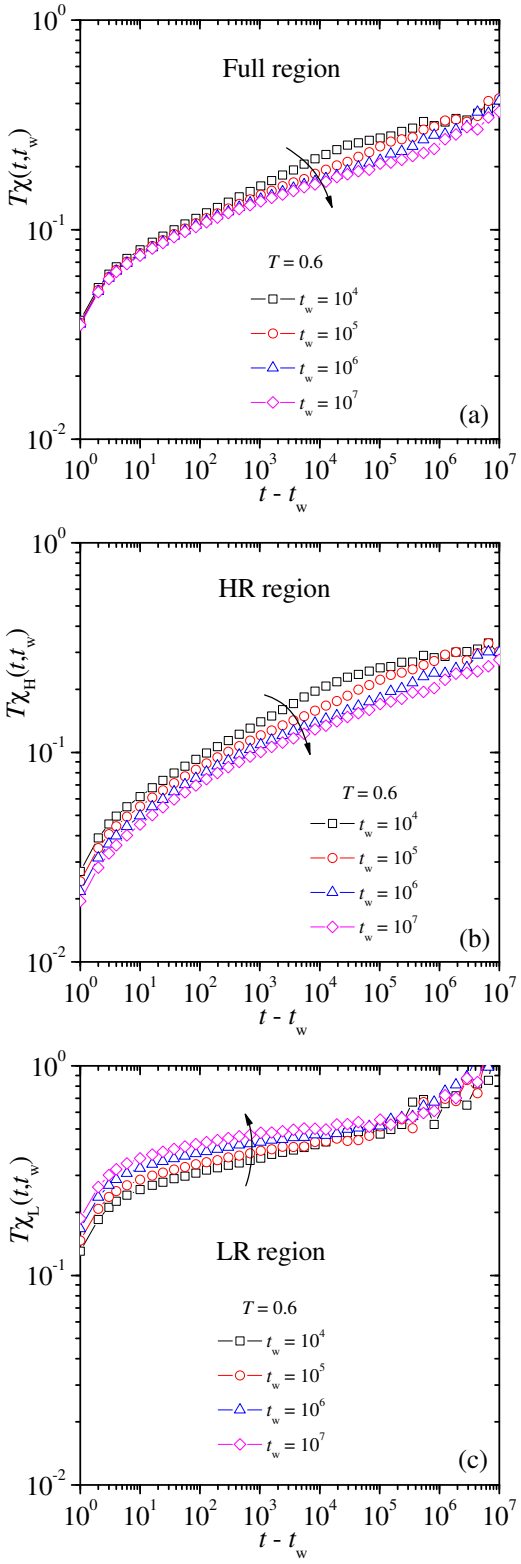

Fig. 4. The integrated response functions (a) χ, (b) $\chi_{\rm H}$, and (b) $\chi_{\rm L}$. Curves are for $T = 0.6$ and different waiting times as indicated. The arrows emphasize how such functions evolve with increasing $t_{\rm w}$.

and (c). As before for the correlation functions calculated over the full and the HR regions, χ and $\chi_{\rm H}$ show a similar trend although in this case both fall instead of rising with increasing $t_{\rm w}$. This is typical of nonequilibrium systems which develop a sort of domain-growth process (for example coarsening in ferromagnets), where the domains poorly respond to an external perturbation while the walls that separate them are composed of spins that easily align with the applied field [23]. As the system evolves these domain walls tend to disappear and therefore the response function must decrease for long times. Again our numerical results reinforce the idea that a domain-growth process could be taking place inside the backbone.

On the other hand, for short times the response of spins within the LR region is larger than for the HR region, see Fig. 4 (c). Besides, $\chi_{\rm L}$ increases with increasing $t_{\rm w}$, contrary to what happens for χ and $\chi_{\rm H}$. This behavior shows that the LR region become disordered and probably is not able to support an ordered phase. In the next section, the analysis of the combined effect of the correlation and the integrated response functions, the FDT plots, will be crucial to understand the overall physical behavior of each region.

3.2 FDT plots

The full correlation and integrated response functions are related through a quasi-fluctuation-dissipation theorem

$$T\chi(t,t_{\rm w}) = X\left[1 - C(t,t_{\rm w})\right], \qquad (5)$$

where X is the fluctuation-dissipation ratio (FDR) [46]. A useful representation of this equation is a parametric plot, or "FDT plot", of $T\chi$ vs. C [34,35]. At thermodynamic equilibrium when the FDT holds, the FDR is $X = 1$ and the parametric plot shows a linear relation with a slope of -1. In this case the correlation and the integrated response functions depend on $\Delta t = t - t_{\rm w}$. On the other hand, in a nonequilibrium situation the FDT does not longer hold and two regimes are observed: for $t/t_{\rm w} \ll 1$ the system shows quasi-equilibrium with $X = 1$, while for $t/t_{\rm w} \gg 1$ a violation of the FDT is observed with $X < 1$. The behavior of X for $t/t_{\rm w} \gg 1$ allows for a simple classification of nonequilibrium systems into three main categories: (*i*) the value $X = 0$ is related to coarsening systems, (*ii*) a constant $X < 1$ value is associated with structural glasses, and (*iii*) a decreasing monotonic $0 < X < 1$ function corresponds to spin glasses.

In Fig. 5 (a) we can see the FDT plot for $T = 0.6$ and different waiting times. After the quasi-equilibrium regime, the curves deviates from the straight line of slope -1 and show a continuous variation of the FDR (see their derivatives in the inset) which, as noted above, is associated to spin glasses [32,33]. On the other hand, Fig. 5 (b) shows the FDT plot of the spins belonging to the HR region for different values of $t_{\rm w}$. Notice the similarity with the curves in Fig. 5 (a). There does not seem to be differences between the full system and the HR region.

Nevertheless, a rather more striking behavior is observed for the FDT plot within the LR region, Fig. 5 (c).

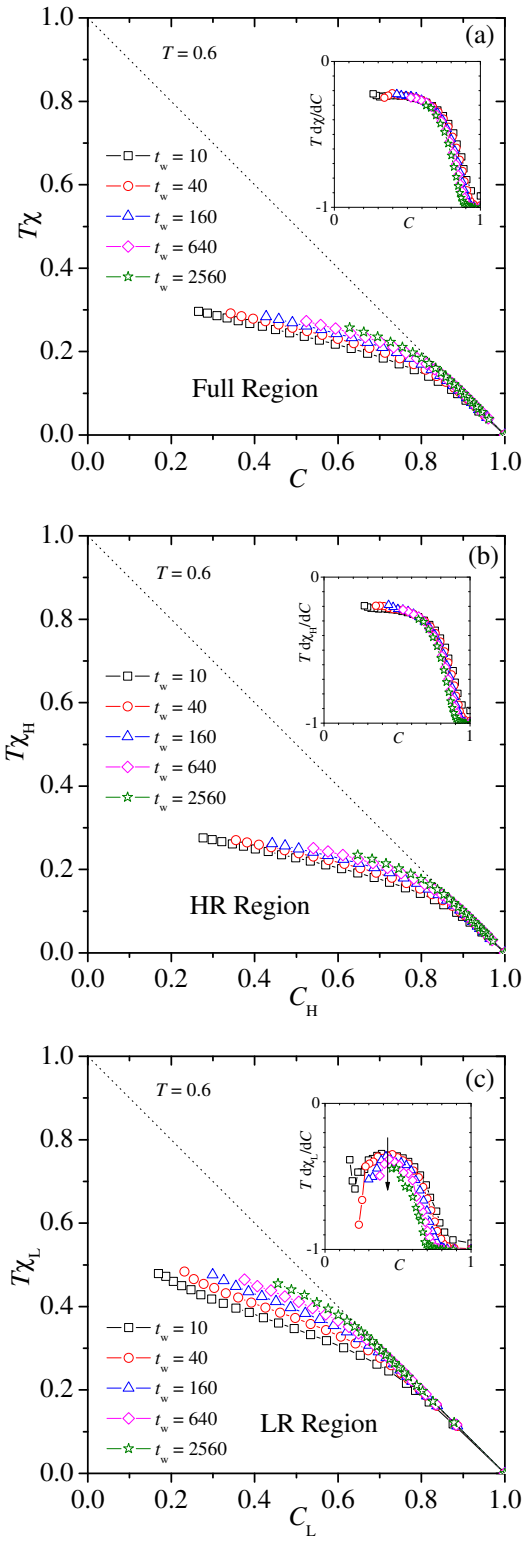

Fig. 5. The FDT plots for (a) the Full, (b) the HR, and (c) the LR regions at $T = 0.6$ and for different $t_{\rm w}$ as indicated. The insets show the slope of these curves as function of C.

We expect this set to behave like the spins outside the backbone in the 3D EAB model, i.e. fulfill FDT ($X \to 1$)

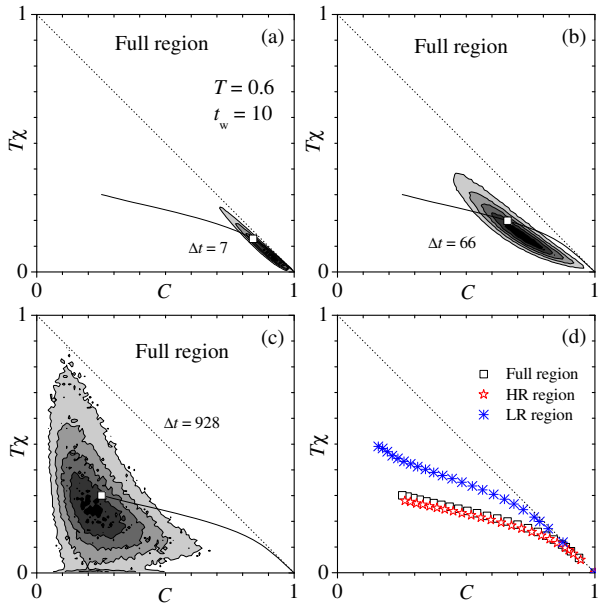

Fig. 6. Panels (a), (b), and (c) show the map plots of the JPD for, respectively, $\Delta t = 7$, 66, and 928, together with the corresponding FDT plots (solid curves). Dark (bright) areas denote high (low) density points. The open squares indicates the position, for each Δt, of the first moment of the JPD. Panel (d) shows the FDT plots for the full, the HR, and the LR regions.

for long times. In fact, as shown in the inset of this figure, the slope of these FDT curves tend to -1 for increasing $t_{\rm w}$.

In order to further analyze how the heterogeneities arise in the violation of the FDT, we follow the lines of Ref. [22]. First, we note that the full correlation function (2) can be rewritten as

$$C(t,t_{\rm w}) = \left[\frac{1}{N}\sum_{i=1}^{N}\widetilde{C}_i(t,t_{\rm w})\right]_{\rm av}, \qquad (6)$$

where

$$\widetilde{C}_i(t,t_{\rm w}) = \langle \sigma_i(t)\sigma_i(t_{\rm w})\rangle \qquad (7)$$

is the thermal average of a single spin correlation function. The same is true for the integrated response function (3),

$$\chi(t,t_{\rm w}) = \left[\frac{1}{N}\sum_{i=1}^{N}\widetilde{\chi}_i(t,t_{\rm w})\right]_{\rm av}. \qquad (8)$$

Then, the sample average of the joint probability distribution (JPD), $\rho(\widetilde{C},T\widetilde{\chi},t,t_{\rm w})$, allows us to visualize clearly how each spin contributes to C and χ. The full correlation and integrated response functions can be recovered by simple integration,

$$C(t,t_{\rm w}) = \int d\widetilde{C}\int d\widetilde{\chi}\;\rho(\widetilde{C},T\widetilde{\chi},t,t_{\rm w})\widetilde{C} \qquad (9)$$

and

$$\chi(t,t_{\rm w}) = \int d\widetilde{C}\int d\widetilde{\chi}\;\rho(\widetilde{C},T\widetilde{\chi},t,t_{\rm w})\widetilde{\chi}. \qquad (10)$$

Figures 6 (a)-(c) show different map plots of the JPD at $T = 0.6$ and for $t_w = 10$. The sequence represents the evolution of this distribution for increasing Δt, together with the corresponding FDT plots (solid curves). Also, for each case, the corresponding coordinates of the first moment of the JPD given by Eqs. (9) and (10) are shown. We emphasize that these map plots were calculated for 10^3 samples and, in order to obtain a converged distribution it was necessary to carry out 10^4 independent runs [1].

At very short Δt into the quasi-equilibrium regime, Fig. 6 (a) shows that the JPD is compact and has an elongated shape oriented along the straight line of slope -1. This behavior can be attributed exclusively both, to the pronounced fall of the correlation function and to the strong response to an external perturbation, that is observed for short times within the LR region. However, with increasing Δt the distribution widens in all directions reflecting the increase of dynamical heterogeneities [see Figs. 6(b) and (c)]. This broadening of the JPD can be interpreted analysing separately the behavior of the entire system, the backbone and its complement. In Fig. 6 (d) we can see the FDT plots for the full ($T\chi$ vs. C), the HR ($T\chi_{\rm H}$ vs. $C_{\rm H}$), and the LR ($T\chi_{\rm L}$ vs. $C_{\rm L}$) regions. The first two show a similar flattening trend, but the LR region shows a pronounced tendency towards equilibrium behavior. This result reinforces the idea proposed in Ref. [22], that the complement of backbone remains in a paramagnetic phase even below the critical temperature.

3.3 Flipping time distribution

Finally, we shall focus on the mean flipping time distribution as an effective direct way to analyze the strong time-scale separations observed in the EAG model. For each sample, we measure the number of flips, $N_{\rm F}$, done by every spin within a time window extending from t_w to t, being $\Delta t = t - t_w$. The mean flipping time $\tau_{\rm F}$ for a given t_w and t is defined as the time window size divided by the number of flips: $\tau_{\rm F}(t, t_w) = \Delta t/N_{\rm F}$ [31]. We calculate the mean flipping time distribution for each sample and then we average these to compute $P(\ln \tau_{\rm F})$. As in Ref. [31], we use a logarithmic scale for the argument due to the broadness of this distribution.

Instead of Glauber, we choose to work with a Metropolis dynamics whose transition rate is given by [47]

$$W_{\rm M} = \min\{1, \exp(-\beta \Delta H)\}. \qquad (11)$$

Although both dynamics belong to the same universality class (Model A) [48], we prefer to use Metropolis to make a direct comparison with the results reported in Refs. [31, 20, 23] for the EAB model.

[1] The product $\sigma_i(t)\sigma_i(t_w)$ can take only two values, ± 1. But the average of this quantity, the single spin correlation function (7), has a real value with a standard deviation which is sufficiently small ($\ll 1$), if an adequate number of independent runs are used to calculate it. The same is true for the single response function.

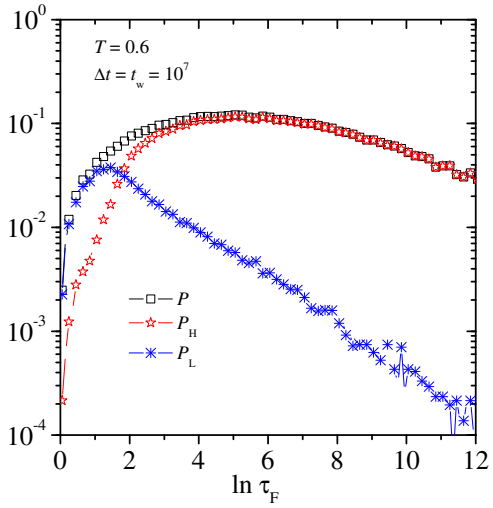

Fig. 7. The mean flipping time distribution for $\Delta t = t_w = 10^7$ at $T = 0.6$. Figure shows a comparison between the full distribution P and the corresponding ones for the HR and the LR regions, $P_{\rm H}$ and $P_{\rm L}$, respectively.

When analyzing the 3D EAB model, Ricci-Tersenghi and Zecchina showed that the flipping time distribution widens as the temperature decreases and develops a visible two-peaked structure [31]. As the temperature decreases, the peak located at high flipping times, corresponding to the slow degrees of freedom, moves towards higher values in accordance with an activation process of energy $\varepsilon = 4$ [2]. Concurrently, the peak located at small flipping times, which characterizes fast degrees of freedom, does not depend on temperature and is located at $\tau_{\rm F} \approx 1$. This means that the EAB model is composed of a fraction of spins which behave like approximately "free spins", i. e. spins whose flipping does not change the energy and then can be flipped on every time step (the Metropolis rate for accepting these moves is one). Within the backbone picture this set of spins plays an important role because, even well below T_c, it behaves like a paramagnet.

To study the 3D EAG model we compare, as before, the full mean flipping time distribution P with the corresponding ones $P_{\rm H}$ and $P_{\rm L}$ calculated over the sets of spins belonging to the HR and the LR regions. Figure 7 shows these functions at $T = 0.6$ and for $t_w = \Delta t = 10^7$. Although a strong time-scale separation (two-peaked structure) is not observed, we clearly obtain that the LR (HR) region represent very well the fast (slow) degrees of freedom, as in the EAB model

Figure 8(a-c) show the mean flipping time distribution for different temperatures below the critical one, and again for $t_w = \Delta t = 10^7$. For the full set of spins, Fig. 8(a), we observe that as temperature is decreased P becomes broader and more spins begin to flip slowly. The same qualitative behavior is observed for $P_{\rm H}$ in Fig. 8(b). This

[2] For the bimodal Edwards-Anderson model with $\pm J$ couplings, the minimum excitation energy is $\varepsilon = 4J$; here we have taken $J = 1$.

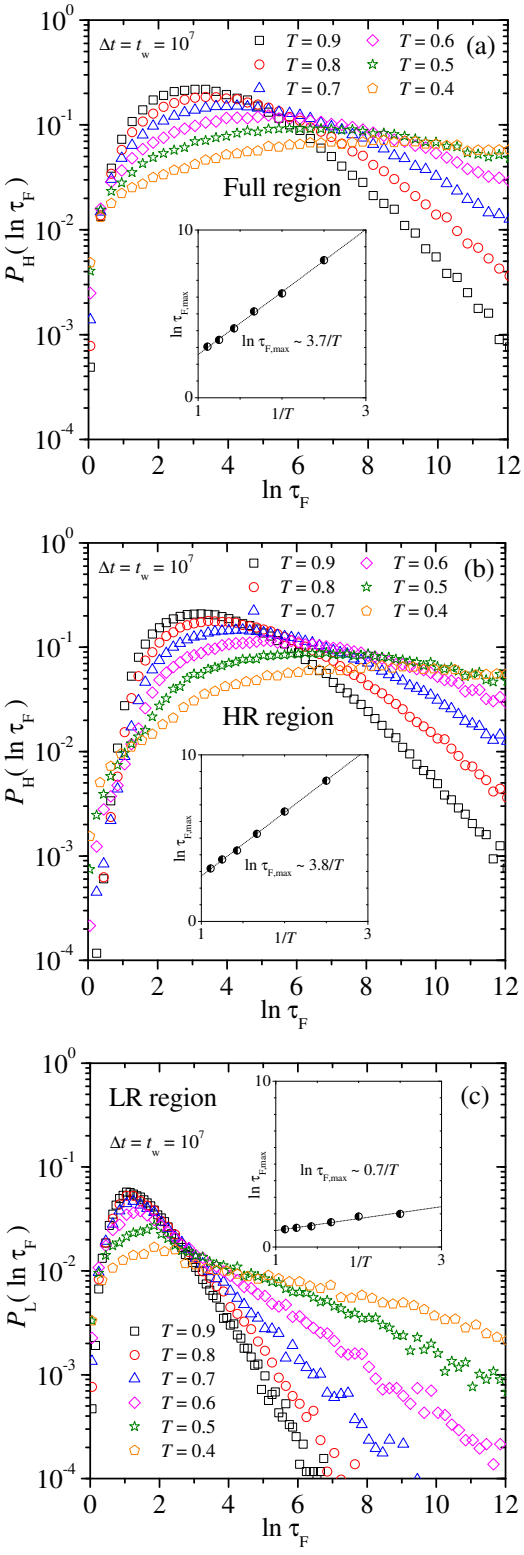

Fig. 8. The mean flipping time distributions (a) P, (b) $P_{\rm H}$, and (c) $P_{\rm L}$ for $\Delta t = t_{\rm w} = 10^7$ and for different temperatures as indicated. The insets present the dependency of $\ln \tau_{\rm F,max}$ with $1/T$ for each region.

is a typical low-temperature behavior observed in several glassy systems. Note also that the single peaks of P and $P_{\rm H}$ depend on temperature as $\ln \tau_{\rm F,max} \sim \varepsilon/T$, with $\varepsilon = 3.7$ and 3.8, respectively (see insets). This behavior is very close to the corresponding one for the slow degrees of freedom of the EAB model, for which the position of the peak for large flipping times scales as $4/T$ [31,20,23]. On the other hand, for the LR region [Figs. 8 (c)] the peak of the distribution $P_{\rm L}$ becomes sharper and scales also as $\ln \tau_{\rm F,max} \sim \varepsilon/T$ but with a smaller value $\varepsilon = 0.7$.

Next, we analyze what happens at constant temperature, $T = 0.6$, with increasing $t_{\rm w}$. For simplicity we only show data for $\Delta t = t_{\rm w}$. As expected, the overall behavior is qualitatively rather similar to that found in the 3D EAB model (see Fig. 4 in Ref. [23]). The full mean flipping time distribution, Fig. 9 (a), approximately preserves its shape as the waiting time increases, although inside and outside the backbone the dynamics is very different. Figure 9 (b) shows that $P_{\rm H}$ is as wide as P but evolves slowly in time, particularly decreasing for small values of $\tau_{\rm F}$ (see arrow in this figure). In other words, eventually some fast spins tend to slow down its flipping rate. On the contrary, Fig. 9 (c) shows that the mean flipping time distribution for the LR region evolves in the opposite direction, i. e., with increasing $t_{\rm w}$ a fraction of the slow spins increases its activity. In Ref. [23], this singular behavior was detected in the 3D EAB model and, by comparing with that observed in the 3D ferromagnetic Ising model, was interpreted as an indirect evidence of the existence of a domain-growth process taking place inside the backbone.

4 Discussion and conclusions

In this work we have analyzed different aspects of the nonequilibrium behavior of the 3D EAG spin glass model. In particular, we have focused on establishing a link between the dynamical and spatial heterogeneities observed on this system.

For each disorder sample realization, spatial heterogeneities are well characterized by the RS, a lattice where each bond J_{ij} has been replaced by its rigidity r_{ij}, a quantity that measures the strengh of the effective interaction between the spins σ_i and σ_j. In the EAB model, the rigidity distribution $F(r)$ is discrete and therefore it allows to separate the system in few components, mainly a backbone and its complement. Previous studies suggest that this backbone is capable of sustaining a ferromagnetic-like order, while the rest of the system remain in a paramagnetic phase, even below the critical temperature [20,21, 22,23,24,25,26]. Remarkably, although the EAG model has a continuous rigidity distribution, we can determine an adequate rigidity threshold, $r_{\rm min} = 1.3$, to separate the system in a backbone and its complement, both having similar topological properties to those found in the bimodal case [27].

As considered in Ref. [49], a different approach could be to study the dynamical heterogeneities by partitioning the rigidity distribution in many sectors. Using this

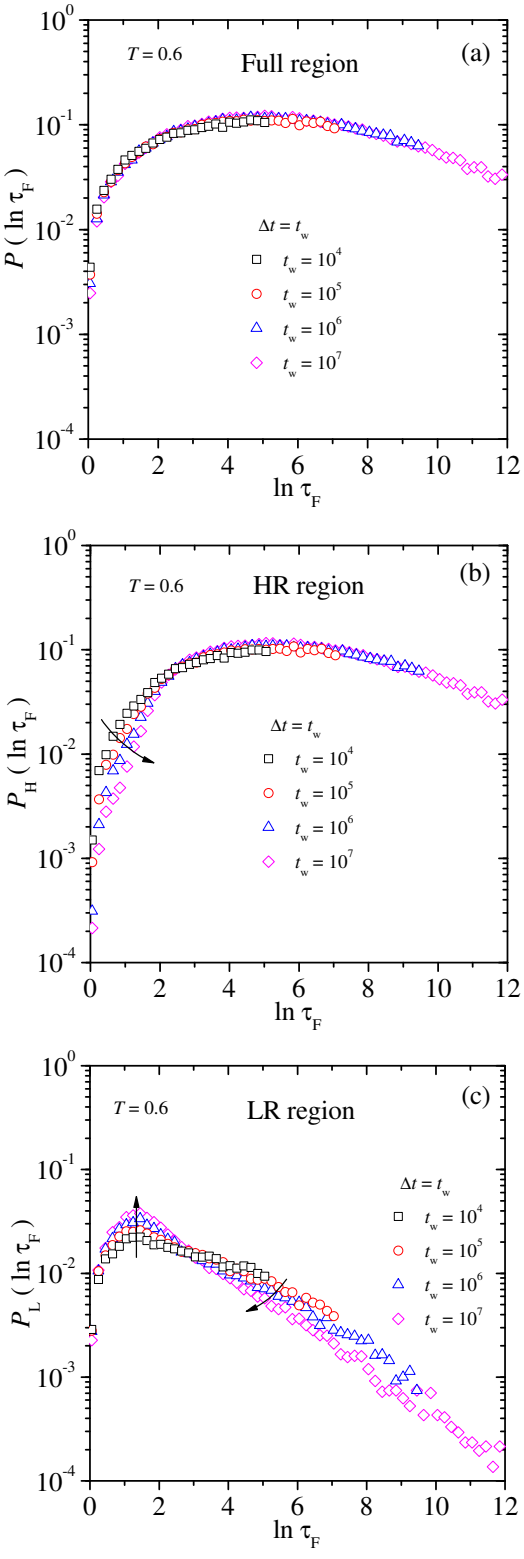

Fig. 9. The mean flipping time distributions for $T = 0.6$ and different waiting times, keeping $\Delta t = t_{\rm w}$. Panels show (a) P, (b) $P_{\rm H}$ and (c) $P_{\rm L}$. The arrows emphasize how such distributions evolve with increasing $t_{\rm w}$.

idea in the 3D EAB model, which has a discrete rigidity distribution with four sectors (corresponding to peaks at $r = 0$, $r = 4$, $r = 8$, and $r = 12$), no significant differences in the physical properties between sectors with $r \geq 4$ are observed. By performing a series of preliminary simulations, we have concluded that this is also true for the EAG model, where we only found qualitative differences when we separate the system into two components.

In Sec. 3, we first studied the correlation and the integrated response functions. While both quantities show a similar trend for the full and the HR region, for the LR region the curves evolve (with increasing waiting time) in opposite directions. In particular, the FDT plots for the latter sector, seems to reinforce the idea that the complement of backbone is paramagnetic at any nonzero finite temperature. If, as proposed in Ref. [22] for the 3D EAB model, the backbone is capable of sustaining a ferromagnetic-like order, then we should observe that the FDT plots tend to a plateau for increasing $t_{\rm w}$. Since the EAG model has a continuous spectrum of energy levels, implying that the rigidity distribution $F(r)$ is also continuous [see Fig. 1(b)], this behavior is probably impossible to observe in such a system within the longer time scales and the larger lattice sizes which can be simulated.

Finally, we analyzed the mean flipping time distribution. For the EAG model $P(\ln \tau_{\rm F})$ is very broad but, unlike the EAB model, does not have a two-peaked structure. Nevertheless, the contributions of the HR and the LR regions resembles the behavior found in the bimodal system. Namely, $P_{\rm H}$ has a single peak that depends on temperature as $\ln \tau_{\rm F,max} \sim 3.8/T$ ($\sim 4/T$ for the backbone of the EAB model), in accordance with an activation process with a characteristic mean energy barrier of $\varepsilon \sim 3.8$. On other hand, $P_{\rm L}$ also has a single peak that depend on $1/T$ but with a smaller slope, $\varepsilon \sim 0.7$. Although this effective energy barrier is nonzero (for the EAB model, the complement of the backbone does not depends on T), notice that it is an order of magnitude smaller than the one corresponding to the HR region.

The comparison between the nonequilibrium dynamics and spatio-temporal heterogeneities in the EAB and EAG models has to be considered with some caution. This comparison, within the backbone picture, is based on the assumption that the bond rigidity r_{ij} is a measure of the true interaction strength (effective interaction) between the pair of spins at sites i and j. Although both are disordered models, the EAB has a discrete rigidity distribution $F(r)$ with only two significant peaks at $r = 0$ (the LR region) and $r = 4$ (this is approximately the HR region; in fact, the backbone is formed by bonds with $r \geq 4$ but the peaks with $r > 4$ are not relevant, see Fig. 1(a)) [27]. As a consequence, this system shows a marked separation between paramagnetic-like and ferromagnetic-like phases, a phenomenon that is most dramatically revealed in the two-peaked structure of the mean flipping time distribution [31,20,23]. Instead, for the EAG model, the time scale heterogeneous behavior is revealed by a very broad rigidity distribution $F(r)$ (notice that the $\ln \tau_F$ scale in Fig. 7 corresponds to a spread of flipping times within five or-

ders of magnitud) and then this phase separation is more subtle and difficult to observe.

In conclusion, we find that the nonequilibrium dynamics of the 3D EAG and EAB models, displays several similitudes when both systems are separated into their main components, the backbone and its complement. For the Gaussian case and below the critical temperature, this latter region shows evident signs of a paramagnetic-like behavior. Instead, within the backbone our data, as for the EAB model, points to the existence of a very slow domain-growth process, most probably with a ferromagnetic-like character.

Author contribution statement

All authors designed the study, analyzed the results, wrote and revised the manuscript. F. R. performed the numerical simulations.

F. Romá acknowledges financial support from CONICET (Argentina) under project No. PIP 112-201301-00049-CO, FONCyT (Argentina) under project PICT-2013-0214, and Universidad Nacional de San Luis (Argentina) under project PROICO P-31216. S. Bustingorry acknowledges partial support by CONICET (Argentina) under Project No. PIP 112-201201-00250-CO.

Appendix: Dynamic behavior for different values of $r_{\min}$

For the 3D EAG model, we have selected a rigidity threshold value of $r_{\min} = 1.3$ that separates the lattice into HR and LR regions. When comparing the number of spins within each region, they look somewhat different: the average fraction of spins within the HR and LR regions are $p \approx 0.91$ and $1 - p \approx 0.09$, respectively, suggesting that the backbone is much larger than its complement. However, note that the backbone is defined in terms of rigidity, which is a bond's property. For the 3D EAG model, in average, the fraction of bonds within the HR and LR regions are $h \approx 0.64$ and $1 - h \approx 0.36$, respectively, and in terms of bond's fraction, the LR region comprises half the size of the HR region. In Ref. [27] it was shown that both regions percolate over the system, and thus they are composed of at least one cluster whose size is of the order of N.

When varying the value of $r_{\min}$ the fractions h and p change, as shown in Table 1. However, the qualitative behavior of the spins belonging to the HR and LR regions do not change when $r_{\min}$ is in the range $0.6 < r_{\min} < 2.0$. As an example, we show in Figs. 10 (a) and (b) that for $r_{\min} = 1.0$, the correlation functions $C_{\rm H}$ and $C_{\rm L}$ do not suffer significant changes [compare these figures with Figs. 3 (b) and (c)]. Also, we observe a similar trend if we take $r_{\min} = 2.0$, Figs. 11 (a) and (b). For values of $r_{\min} > 2$, both $C_{\rm H}$ and $C_{\rm L}$ behave in the same way that the full correlation functions C (for simplicity these curves are not shown here). On the other hand, for $r_{\min} < 0.6$ (below the range $[0.6 - 2.0]$), we can still observe curves like those shown in Figs. 10 and 11 but in this case, where

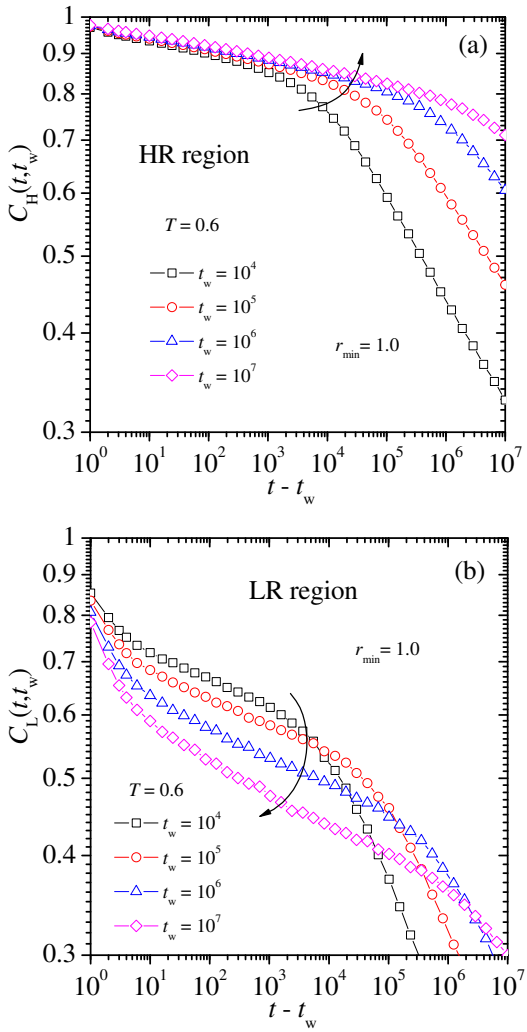

Fig. 10. The correlation functions (a) $C_{\rm H}$ and (b) $C_{\rm L}$ at $T = 0.6$ and for different waiting times as indicated. The HR and LR regions have been delimited choosing $r_{\min} = 1.0$. The arrows emphasize how such functions evolve with increasing $t_{\rm w}$.

Table 1. Approximate values of the bonds fraction h and the spins fraction p for different values of $r_{\min}$.

$r_{\min}$	h	p
0.1	0.97	1.00
0.5	0.86	0.98
1.0	0.72	0.94
1.3	0.64	0.91
2.0	0.48	0.81
3.0	0.29	0.62
4.0	0.16	0.41

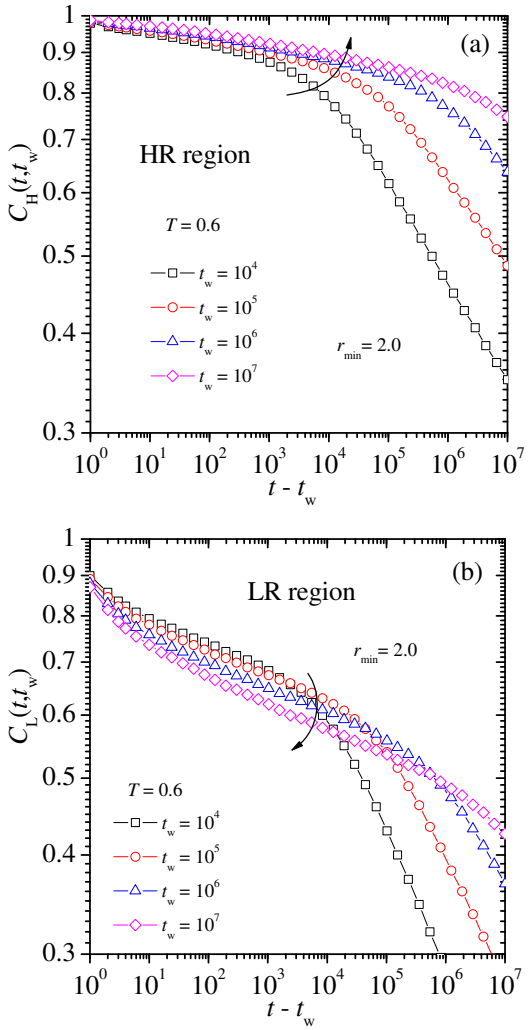

Fig. 11. The same as for Figs. 10 (a) and (b) but now for $r_{\min} = 2.0$.

the size of the LR region is very small (see Table 1), the behavior of $C_{\rm L}$ corresponds to a few quasi-free spins (spins that can flip with a negligible energy cost) which represent only a fraction of the true (larger) LR region. The remaining observables show a similar behavior with respect to changes in the value of $r_{\min}$.

References

1. K. Binder, A. P. Young, Rev. Mod. Phys. **58** 801 (1986).
2. J. A. Mydosh, *Spin Glasses: An Experimental Introduction* (Taylor & Francis, London, 1993).
3. J. L. Tholence, R. Tournier, J. Physique **35**, C4-229 (1974).
4. E. P. Wohlfarth, Physica **86-88B**, 852 (1977).
5. A. F. J. Morgownik, J. A. Mydosh, Phys. Rev. B **24**, 5277 (1981).
6. B. H. Verbeek, G .J. Nieuwenhuys, J. A. Mydosh, C. van Dijk, B. D. Rainford, Phys. Rev. B **22**, 5426 (1980).
7. M. A. Ruderman, C. Kittel, Phys. Rev. B **96**, 99 (1954).
8. T. Kasuya, Prog. Theor. Phys. **16**, 45 (1956).
9. K. Yosida, Phys. Rev. **106**, 893 (1957).
10. G. Parisi, Phys. Rev. Lett. **43**, 1754 (1979).
11. G. Parisi, Phys. Rev. Lett. **50**, 1946 (1983).
12. D. S. Fisher, D. A. Huse, Phys. Rev. Lett. **56**, 1601 (1986).
13. S. F. Edwards, P. W. Anderson, J. Phys. F **5**, 965 (1975).
14. G. Toulouse, Commun. Phys. (London) **2**, 115 (1977).
15. F. Barahona, R. Maynard, R. Rammal, J. P. Uhry, J. Phys. A: Math. Gen. **15**, 673 (1982).
16. T. Klotz, S. Kobe, J. Phys. A **27**, L95 (1994).
17. J. F. Valdés, J. Cartes, E. E. Vogel, S. Kobe, T. Klotz, Physica A **257**, 557 (1998).
18. E. E. Vogel, S. Contreras, M. A. Osorio, A. J. Ramirez-Pastor, F. Nieto, Physica A **266**, 425 (1999).
19. A. J. Ramirez-Pastor, F. Nieto, S. Contreras, E. E. Vogel, Physica A **283**, 94 (2000).
20. F. Romá, S. Bustingorry, P. M. Gleiser, Phys. Rev. Lett. **96**, 167205 (2006).
21. F. Romá, S. Risau-Gusman, A. J. Ramirez-Pastor, F. Nieto, E. E. Vogel, Phys. Rev. B **75**, 020402(R) (2007).
22. F. Romá, S. Bustingorry, P. M. Gleiser, D. Domínguez, Phys. Rev. Lett. **98**, 097203 (2007).
23. F. Romá, S. Bustingorry, P. M. Gleiser, Phys. Rev. B **81**, 104412 (2010).
24. F. Romá, S. Risau-Gusman, A. J. Ramirez-Pastor, F. Nieto, E. E. Vogel, Phys. Rev. B **82**, 214401 (2010).
25. M. L. Rubio Puzzo, F. Romá, S. Bustingorry, P. M. Gleiser, Europhysics Letters **91**, 37008 (2010).
26. M. L. Rubio Puzzo, F. Romá, S. Bustingorry, P. M. Gleiser, J. Stat. Mech. P09017 (2010).
27. F. Romá, S. Risau-Gusman, Phys. Rev. E **88**, 042105 (2013).
28. H. G. Katzgraber, M. Körner, A. P. Young, Phys. Rev. B **73**, 224432 (2006).
29. F. Romá, Phys. Rev. B **82**, 212402 (2010).
30. D. Stauffer, *Introduction to Percolation Theory* (Taylor & Francis, London, 1985).
31. F. Ricci-Tersenghi, R. Zecchina, Phys. Rev. E **62**, R7567 (2000).
32. A. Barrat, Phys. Rev. E **57**, 3629 (1998).
33. F. Ricci-Tersenghi, Phys. Rev. E **68**, 065104(R) (2003).
34. L. F. Cugliandolo in, *Slow Relaxations and Nonequilibrium Dynamics in Condensed Matter*, edited by J.-L. Barrat et al. (Springer, Berlin, 2002).
35. A. Crisanti, F. Ritort, J. Phys. A: Math. Gen. **36**, R181 (2003).
36. E. E. Ferrero, F. Romá, S. Bustingorry, P. M. Gleiser, Phys. Rev. E **86**, 031121 (2012).
37. A. Montanari, F. Ricci-Tersenghi, Phys. Rev. B **68**, 224429 (2003).
38. D. J. Perez-Morelo, A. J. Ramirez-Pastor, F. Romá, Physica A **391**, 937 (2012).
39. A. J. Ramirez-Pastor, F. Romá, F. Nieto, E. E. Vogel, Physica A **336**, 454 (2004).
40. C. Geyer, *Computing Science and Statistics: Proceedings of the 23rd Symposium on the Interface* (American Statistical Association, New York, 1991), p. 156.
41. K. Hukushima, K. Nemoto, Phys. Soc. Jpn. **65**, 1604 (1996).
42. J. L. Moreno, H. G. Katzgraber, A. K. Hartmann, Int. J. Mod. Phys. C **14**, 285 (2003).
43. F. Romá, S. Risau-Gusman, A. J. Ramirez-Pastor, F. Nieto, E. E. Vogel, Physica A **388**, 2821 (2009).
44. C. Chatelain, J. Phys. A: Math. Gen. **36**, 10739 (2003).

45. R. J. Glauber, J. Math. Phys. **4**, 294 (1963).
46. L. F. Cugliandolo, J. Kurchan, L. Peliti, Phys. Rev. E **55**, 3898 (1997).
47. N. Metropolis, A. W. Rosenbluth, N. M. Rosenbluth, A. H. Teller, E. Teller, J. Chem. Phys. **21**, 1087 (1953).
48. P. C. Hohenberg, B. Halperin, Rev. Mod. Phys. **49**, 435 (1977).
49. M. Baity-Jesi *et al.*, J. Stat. Mech. P05014 (2014).